Nanoscale

www.rsc.org/nanoscale

Volume 4 | Number 23 | 7 December 2012 | Pages 7283–7602

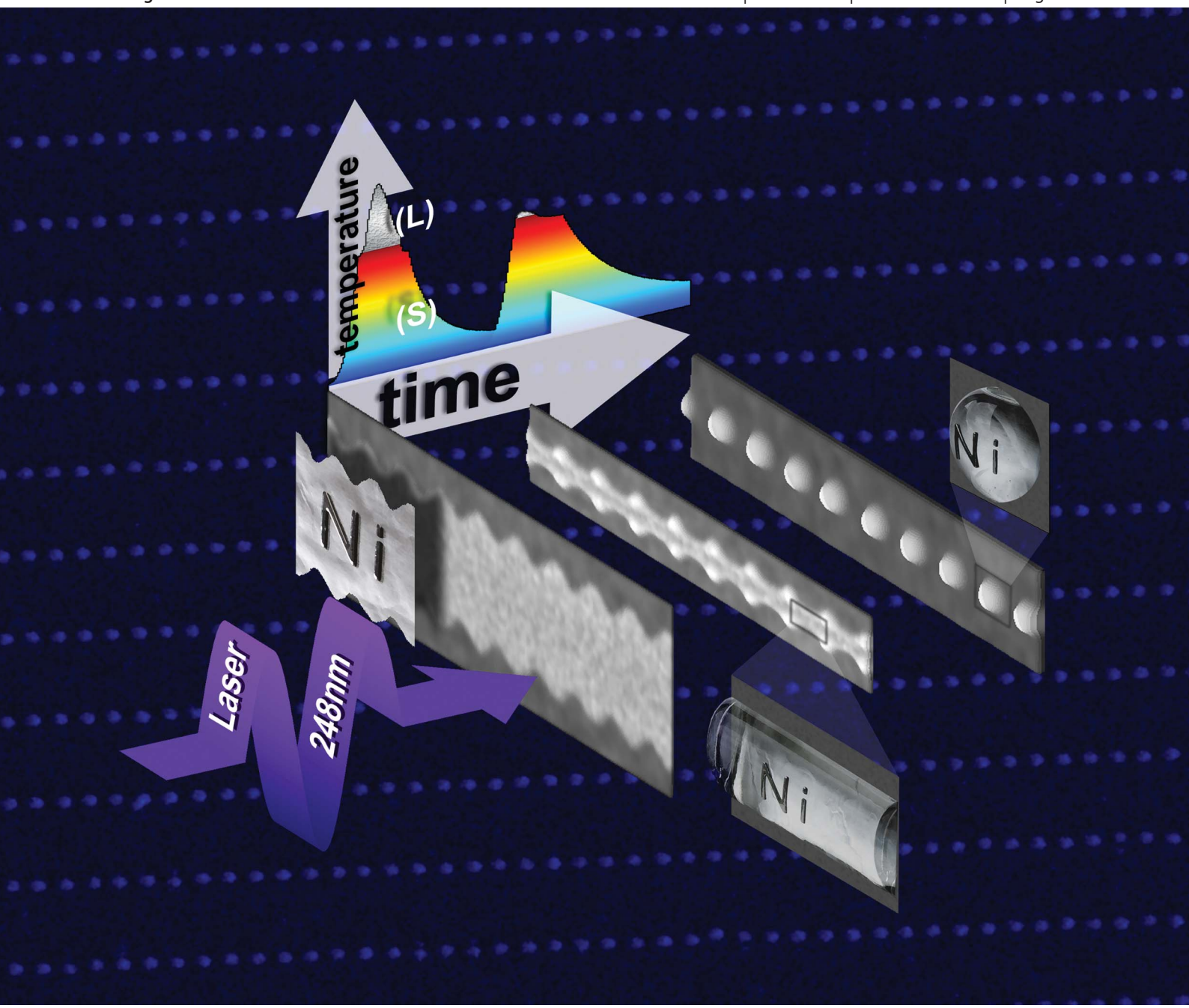

ISSN 2040-3364

RSC Publishing

PAPER
Fowlkes *et al.*
Parallel assembly of particles and wires on substrates by dictating instability evolution in liquid metal films

NCNST

Nanoscale

Dynamic Article Links

Cite this: *Nanoscale*, 2012, **4**, 7376

www.rsc.org/nanoscale

PAPER

Parallel assembly of particles and wires on substrates by dictating instability evolution in liquid metal films†

Jason D. Fowlkes,*[a] Lou Kondic,[b] Javier A. Diez,[c] Alejandro G. González,[c] Yueying Wu,[d] Nick A. Roberts,[d] Cliff E. McCold[e] and Philip D. Rack[ad]

Received 26th June 2012, Accepted 14th September 2012
DOI: 10.1039/c2nr31637d

Liquid metal wires supported on substrates destabilize into droplets. The destabilization exhibits many characteristics of the Rayleigh–Plateau model of fluid jet breakup in vacuum. In either case, breakup is driven by unstable, varicose surface oscillations with wavelengths greater than the critical one (λ_c). Here, by controlling the nanosecond liquid lifetime as well as stability of a rivulet as a function of its length by lithography, we demonstrate the ability to dictate the parallel assembly of wires and particles with precise placement.

Introduction

Metal nanowires and nanoparticles have emerged as central features in the function of various magnetic[1,2] and plasmonic[3] devices as well as molecular-scale electronic elements.[4] Conventional lithography approaches, such as photon and focused electron beam methods, are typically used to obtain imperfect replicas of these features such as rectangular strips (for model nanowires) and cylinders (for spherical particles) due to the constraint of a two-dimensional exposure pattern; photon/electron exposure of thin polymeric resists defines the desired nanostructure pattern in the substrate plane, yet cannot contour the out-of-plane (z) dimension. Only the thickness of the metal is controlled in the z-dimension. Yet, curvature plays a key role in nanoscale behavior such as enhanced light capture in photovoltaic thin films using metallic nanocaps/particles.[5,6] To enhance functionality, new and complementary methods have emerged to produce nanostructures with the desired nanoscale shape and geometry such as nanoimprint lithography (NIL),[7] nanoscale origami,[8,9] template stripping,[10] colloidal lithography,[11] laser-assisted direct imprinting (LADI),[12] self-perfection by liquefaction (SPEL)[13] and directed, pulsed laser induced dewetting (PLiD).[14,15] The latter method makes use of the mature infrastructure of conventional lithography methods to specify the initial material geometry which ultimately controls the liquid flow during pulsed laser melting.[14,16] This method facilitates either self- or directed- assembly *via* the development of fluid instabilities resulting in ordered metallic spherical caps on substrates.[14] Although a "spherical cap" morphology results, in the following we refer to this morphology using the more general terminology of a "particle". Here, we demonstrate that directed assembly can be further extended to facilitate the parallel, simultaneous assembly of true wire and particle geometries supported on substrates.

The demonstration of self assembly across multiple length scales or the parallel assembly of multiple material features simultaneously constitute the next step towards practical materials assembly. Regarding the former, Duan and Berggren[17] has recently demonstrated directed assembly using a combination of electron beam lithography and capillary force induced nanocohesion. Lopes and Jaeger[18] has produced the hierarchical self-assembly of metal nanostructures on diblock copolymer scaffolds yielding self-assembled nanochains. The confluence of top-down and bottom-up assembly has proven a powerful method to produce large-area, hierarchical nanostructures.[19,20] There are however, fewer demonstrations of parallel assembly, especially for the cases of metallic materials. Cho *et al.* have demonstrated the ability to assemble three-dimensional materials such as cylinders, boxes and triangles[21] in a single assembly step where the liquefaction of a metal hinge plays a key role.[9,22,23]

We have recently demonstrated the *organized* spatial assembly of metal particles on both Si[14,24,25] and SiO_2-coated wafer surfaces.[26] The surface energy ($\gamma \approx 1$ N m^{-1}) and viscous dissipation (viscosity $\mu \approx 10^{-3}$ Pa s) of liquid metals interact during hydrodynamic flow producing nanosecond assembly

[a]*Center for Nanophase Materials Sciences, Oak Ridge National Laboratory, Oak Ridge, TN, 37381-6493, USA. E-mail: fowlkesjd@ornl.gov*
[b]*Center for Applied Mathematics and Statistics, Department of Mathematical Sciences, New Jersey Institute of Technology, Newark, New Jersey, 07102, USA*
[c]*Instituto de Física Arroyo Seco, Universidad Nacional del Centro de la Provincia de Buenos Aires, Pinto 399, 7000, Tandil, Argentina*
[d]*Materials Science and Engineering Department, The University of Tennessee, Knoxville, TN, 37996-2200, USA*
[e]*Chemical Engineering & Materials Science, University of California, Davis, 95616, USA*

† Electronic supplementary information (ESI) available: A typical time–temperature profile at the liquid Ni–SiO_2 substrate interface, induced by a single laser pulse, is provided as well as estimates of the temporal evolution of select stable and unstable surface perturbations on liquid Ni rivulet surfaces. See DOI: 10.1039/c2nr31637d

times when the minimum spatial dimension of the liquid feature is on the order of nanometers. For example, the characteristic hydrodynamic velocity $V_h = \gamma/\mu$ for liquid Ni is ~440 nm ns^{-1}. Thus, controlling the melt or liquid lifetime at the nanosecond timescale is paramount for controlled assembly. Conveniently, this can be achieved *via* standard nanosecond pulsed laser irradiation, but requires thin film thicknesses less than ~30 nm because larger thicknesses increase the requisite laser fluence and can lead to severe out of plane temperature gradients.

For PLiD, a key feature of the assembly method is the formation of a liquid metal rivulet on the substrate surface. A "rivulet" is defined as a fluid stream deposited on a substrate that is similar to a cylinder truncated by the substrate, parallel to its axis. The rivulet geometry facilitates the evolution of a "modified"[27–29] form of the Rayleigh–Plateau (RP) fluid instability where the substrate and the contact lines affect the behavior of the instability. While the RP instability was originally derived specifically for the case of a fluid jet suspended in vacuum/vapor,[30,31] the liquid–substrate interaction controls the wetting angle of the rivulet on the substrate (θ) which ultimately influences the RP instability.[29] The rivulet ultimately breaks up into a linear chain of droplets as the instability develops. Upon cooling the droplets re-solidify as particles.

Until recently, such demonstrations of particle formation were limited to a *correlated*, but highly dispersed self-assembly process where the RP instability was allowed to freely evolve yielding linear chains of droplets.[12,13,32–36] The critical rivulet radius is defined by the width and thickness of the patterned thin film strip. This led to the formation of a linear chain of particles but with an ill-defined particle size and pitch since there is a large dispersion of the unstable surface waves/perturbations that induce breakup. Fig. 1a shows the growth rate spectrum $\omega(\lambda)$ of surface perturbations as a function of wavelength (λ) (black curve) for a liquid Ni rivulet with a radius of 112 nm, a width of 210 nm and a contact angle with the underlying SiO_2 film of 69°. The growth rate curve was calculated using linear stability analysis (LSA) which includes the effect of the substrate on the RP instability.[15,29] These perturbations either grow (*positive value of the growth rate* ω) or decay (*negative value of* ω) depending on whether the wavelength of the mode is above or below a critical wavelength (λ_c).

A predominant, or mean, droplet pitch emerges since the dispersion curve has a global, positive maximum value indicated by the green line in Fig. 1a. This observation has led to several exhibitions of metal droplet assembly on surfaces.[32–34] However, the droplet pitch (and consequently the particle size) exhibits a large variation due to the breadth of the dispersion curve. As a result, a host of unstable modes simultaneously influences rivulet breakup producing disorder in the final droplet spacing. The relationship between the dispersion curve and the final particle pitch is clear; the wavelength and phase of unstable modes develop dictating the spatial profile of rivulet breakup. Particles form at the peaks of the unstable modes, owing to the fact that the rivulet pinches-off at wave troughs. Mass flows from the troughs to peaks. Recently, we demonstrated that by lithographically imposing a synthetic, unstable perturbation on the initial rivulet (also see illustration in Fig. 1b), we could direct assembly toward a precise nanoparticle size and spacing by ensuring that only a single unstable mode facilitates breakup.[14]

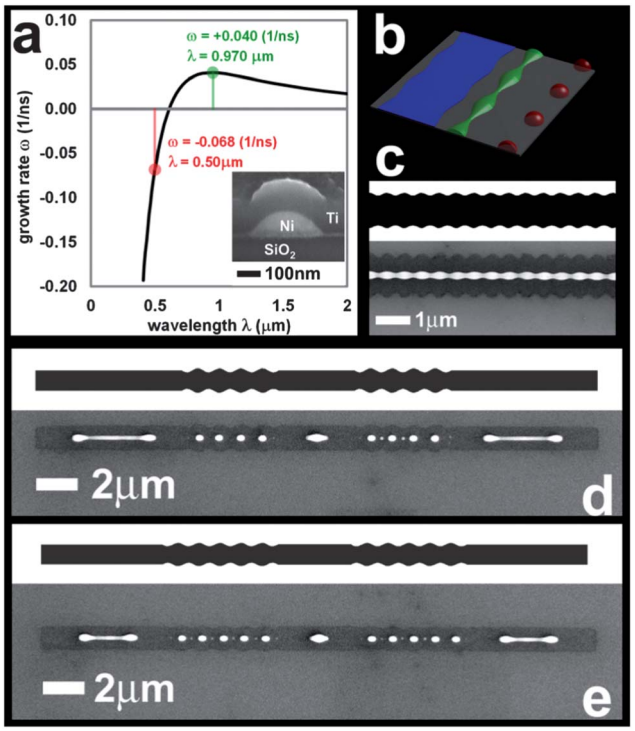

Fig. 1 (a) The dispersion relation $\omega(\lambda)$ for varicose perturbations of a Ni rivulet supported on a SiO_2 surface. The Ni rivulet had a contact width of 210 ± 7 nm, a radius of 112.5 ± 7 nm and a wetting angle of 69° ± 7° with respect to the SiO_2 substrate (see inset). The growth rate of an unstable (λ = 0.970 μm, green line and data point) and stable (λ = 0.500 μm, red line and data point) mode are superimposed. (b) A computer aided design of the thin film strip (blue) used to explore unstable mode propagation. The thin film strip has a mean width of 1.10 ± 0.015 μm, a thickness of 10 ± 1 nm, an edge sinusoid with a wavelength of 0.970 ± 0.015 μm and an amplitude of A_o = 50 ± 7 nm. Shown are 3 periods (Λ) of the thin film strip. A rivulet (green) is obtained from the thin film strip upon pulsed laser melting. (c) Pulsed laser induced melting of a thin film strip with a laser fluence of 220 ± 0.010 mJ cm^{-2}, using 10 laser pulses, induced the formation of the rivulet morphology for a thin film strip patterned with the stable, λ = 0.500 ± 0.015 μm mode. The CAD is also shown for the original thin film strip. The perturbed rivulet is seen as the bright oscillating feature. (d) The combination of an unstable, synthetic mode (λ = 0.970 μm) and a straight, unperturbed section along the thin strip leads to the formation of particles and wires, following re-solidification. (e) This image, when compared with (d), highlights the sensitivity of the parallel assembly process – by patterning one additional period of the unstable mode leads to one additional particle in the unstable segment of the rivulet.

Notably, Hagedorn *et al.*[37] have demonstrated computationally the controlled breakup of a fluid thread in a confined microfluidic channel.

Here, we extend this directed assembly model by imposing both stable and unstable modes (wavelengths) in order to simultaneously assemble precisely positioned wires and particles. Specifically we will show: (1) by lithographically templating the initial geometry of the solid metal, that we can direct the parallel assembly of wires and particles; (2) the parallel assembly is enabled by careful consideration of the liquid phase dynamics of the rivulet formation and the instability development; and (3) that the assembly dynamics can be rationalized by linear stability

analysis of the modified Rayleigh–Plateau instability of the liquid metal. This parallel assembly approach could be used for instance in the assembly of conducting metal nanowire contacts and plasmonic nanoparticle arrays for advanced photovoltaic architectures.[5]

Experimental methods

Electron beam lithography

Ni thin film strips were defined on SiO_2-coated, Si wafers using electron beam lithography followed by direct current magnetron sputtering. The silicon oxide thickness was 100 nm. Focused electron beam exposure at 20 keV and 120 pA was conducted using an FEI Nova 600 dual beam microscope. A poly(methyl methacrylate) (PMMA), positive tone electron sensitive resist 495-A4 provided by Shipley was exposed for strip definition. The PMMA resist was spin coated on a substrate with dimensions of roughly 2 cm × 2 cm in area using a substrate rotation speed of 4000 rpm for 60 s. The spin coating process was followed by a 2 min, 180 °C hot plate bake. An exposure dose of 260 μC cm^{-2} was required in order to completely expose the electron resist yielding well-defined thin film strips while also facilitating the ability to define nanoscale sinusoids on the strip edges. Pattern generation was accomplished using Raith Elphy Quantum software which included an electron beam-blanker incorporated on the FEI Nova electron column. Feature dimensions for scanning electron exposure were contracted by 15% in order to replicate CAD dimensions in the lateral coordinate. This mitigated the electron exposure proximity effect which can lead to the unintended exposure of resist outside the strip design. The strip was exposed using an electron beam probe step of 16 nm and a dwell time per exposure pixel of 5.55 μs producing an electron probe exposure velocity of 2.88 mm s^{-1}. The 495-A4 resist development was carried out in a 1 : 3 methyl isobutyl ketone (MIBK)–isopropyl alcohol (IPA) solution for 100 s followed by an IPA rinse that physically revealed the exposed strips in the resist. The strips were exposed completely down to the underlying SiO_2 layer, surrounded by unexposed resist. An 8 s exposure of the Si chip to an oxygen plasma generated in a reactive ion etcher (100 W capacitively coupled plasma, 10 cm^3 min^{-1} O_2 flow rate and a pressure setting of 150 mTorr) was implemented in order to remove any residual electron resist from the electron exposed regions. Metal was then deposited on the patterned substrates and the metal-on-polymer regions lifted-off to create the patterned metal lines.

Ni thin film strip dimensions

Ni thin film strips were patterned with a mean strip width of 1.1 ± 0.015 μm and a length of 20–30 μm. The thin film strip thickness was 10 ± 1 nm. Once melted, the strips transform into rivulets by way of liquid retraction. The characteristic dimensions of the rivulet include radius, width and contact angle with respect to the substrate. Assuming mass conservation, the resulting radius of the rivulet was 112 ± 7 nm, the width was 210 ± 7 nm and the Ni–SiO_2 contact angle was 69° ± 7°. In certain cases, unstable, synthetic perturbations ($\lambda > 0.950$ μm) with a wavelength patterning error of ±0.015 μm were imposed on the initial strip edge where the amplitude of the perturbations were 50 ± 7 nm. In order to generate the perturbation, sinusoids were patterned on both edges of the thin film strip but shifted in phase by π relative to one another in order to produce a varicose oscillation along the strip length. A stable mode ($\lambda = 0.500 \pm 0.015$ μm) was also explored having an amplitude of 50 nm ± 7 nm.

DC magnetron sputtering deposition

An AJA International 200 DC magnetron sputter deposition system was used to deposit the Ni thin film strips. Sputtering was conducted using the constant power deposition mode at 30 W under a constant chamber pressure of 3 mTorr Ar. A static pressure was maintained using a gas flow rate of 25 cm^3 min^{-1}. The resulting sputter rate of Ni was 5.8 nm min^{-1} for a target-to-substrate distance of ~5 cm. A wet, metal lift-off procedure was used to dissolve unexposed resist resulting in the lift-off of the unwanted metal layer surrounding the Ni thin film strip features. The metal lift-off procedure consisted of immersing the substrate chip in acetone for ~1 min. Subsequently, each substrate chip was rinsed in acetone followed by isopropyl alcohol and blown dry using N_2 gas to remove any remaining debris from the substrate. No specific treatments were done to remove the native nickel oxide prior to laser irradiation. As no obvious influences of the native oxide have been observed in the assembly dynamics, we assume that oxygen dissolves into the liquid metal.[38]

Nanosecond, ultraviolet pulsed laser irradiation

A Lambda Physik LPX-305i, KrF excimer laser (248 nm wavelength) was used to irradiate and melt the Ni thin film strip features. The irradiation geometry was such that the substrate surface was normal to the incident laser pulse. As a result, the top surface of the thin film strip was irradiated as well as the surrounding substrate surface. The incident beam size was on the order of ~1 cm^2. Thus, on the scale of the thin film strip the surface of the strip was uniformly irradiated as well as the surrounding substrate surface. The pulse width of the laser beam was ~18 ns. A beam fluence of 220 ± 10 mJ cm^{-2} was used to melt the strips and focusing of the output beam was required in order to achieve this fluence. All samples reported in this work were irradiated with 10 laser pulses. Thin film strips were irradiated with a beam whose cross sectional size (~1 cm^2) was significantly larger than the strip area (~μm^2) leading to uniformly irradiated strips.

Computational methods

Time–temperature simulations of metal liquid lifetime

Finite element, time–temperature simulations were conducted for the case of a 10 nm thick Ni film (27.9 ns liquid lifetime) and the rivulet morphology (average thickness of 52 nm, 13.8 ns liquid lifetime) supported on a 100 nm SiO_2 thermal oxide coated, silicon wafer substrate (ESI 1†). 1D simulations (z,t) were used in place of more time consuming, 2D simulations (z,x,t) based on the fact that 1D simulations have shown satisfactory agreement with experimental results in the past.[14,25,26,39] The Gaussian temporal beam pulse for a fluence of 220 ± 10 mJ cm^{-2} with a beam pulse FWHM = 18 ns was included in the simulation. The simulation techniques have been described in a

previous publication.[14] Time–temperature simulations were also executed at fluences of 210 and 230 mJ cm^{-2} in order to determine the resulting error in simulated liquid lifetimes due to the fluctuating laser fluence of ±10 mJ cm^{-2}. This fluence range yielded a $\Delta t_{liq} = 3.3$ ns liquid lifetime uncertainty for a 10 nm thick strip and a range of $\Delta t_{liq} = 5.9$ ns for the rivulet with a mean height of 52 nm. A further limitation on simulation accuracy results from the use of time-independent values for the heat capacity, thermal conductivity and density in the solid and liquid phases. All liquid lifetime values reported in the Results and discussion section are simulated values. No experimental measurements of the liquid lifetime were conducted for the experiments reported here, thus all estimates are made based on the thermal simulations.

The differences between present simulations, and those reported previously[14] were two-fold; (1) a finite element algorithm was implemented which was found to better enforce Fourier's Law at the Ni–SiO_2 and SiO_2–Si interfaces using the algorithm provided by Silva *et al.*[33] and (2) the rivulet surface reflectivity was estimated assuming an absorbing Ni cylinder suspended in vacuum according to Mie scattering theory. The rivulet geometry was considered by integrating the scattered fraction of light from only 2θ of the cylinder surface where θ is the contact angle of the rivulet with the SiO_2 substrate; 2θ is subtended by the contact width of the rivulet with the substrate along the direction of the incident photon pulse. Equal amounts of transaxial and transradial light were considered to irradiate the rivulet, with respect to the cylindrical axis. In this way, using the Mie scattering approach, it was possible to include the effect of 2D ultraviolet light scattering from the rivulet geometry by including the mean reflectivity of 0.52 for a rivulet of radius $R_o =$ 112 nm in the 1D time–temperature simulation.

Linear stability analysis to predict Rayleigh–Plateau instability development

The modified Rayleigh–Plateau mechanism of rivulet breakup, including the effect of the solid substrate, was derived by applying the lubrication approximation to the Navier Stokes equations.[15,29] This approximation yields the following nonlinear partial differential equation;

$$3\mu\frac{\partial h}{\partial t} + \gamma\nabla\left(h^3\nabla\nabla^2 h\right) + \nabla\left[h^3\nabla\Pi(h)\right] = 0 \qquad (1)$$

where $h(x,y,t)$ is the Ni liquid thickness, μ is the viscosity of the liquid Ni and $\Pi(h)$ represents the disjoining pressure that accounts for the liquid–substrate interaction. Linear stability analysis (LSA) applied to eqn (1) gives predictions for the evolution of small perturbations of the liquid rivulet surface in the form of the dispersion curve ω *vs.* λ shown in Fig. 1a, where ω and λ are the growth rate and wavelength, respectively, of a varicose perturbation of small amplitude.[15,29] A complete discussion of this approach is provided in ref. 15.

Results and discussion

Critical to the simultaneous evolution of both wires and droplets is control over the liquid lifetime. The estimated RP timescale $\tau_R = ((\rho R_o \sin\theta)^3/\gamma)^{1/2} \sim 3$ ns for the rivulet of width $w_o = 2R_o\sin\theta = 210$ nm gives a rough estimate of the required timescale for rivulet breakup. Liquid lifetime control at the nanosecond timescale was achieved using multiple 18 ns FWHM KrF 248 nm laser pulses with controlled incident photon fluence. As will be shown below, a liquid lifetime on the order of tens of nanoseconds was required to realize the combined wire and particle morphology. However, by controlling the amplitude and wavelength of pre-defined synthetic perturbations, this range could be increased, relaxing the liquid lifetime precision required otherwise. This issue will be described in more detail below. A model Ni strip is shown schematically in Fig. 1b (blue feature) which includes a varicose synthetic perturbation.

The thin film strip geometry (blue), subsequent rivulet (green) and particles (red) are schematically shown in Fig. 1b. The thin film strips were converted into rivulets by a single laser pulse (simulated liquid lifetime of 27.9 ns). During this time period the thin film retracted completely to form a rivulet. Each subsequent laser pulse on the rivulet resulted in a shorter liquid lifetime of 13.8 ns (ESI 1†) due to the increased mean thickness of the rivulet (~52 nm) relative to the initial film thickness of 10 nm. The cumulative liquid lifetime for the experiments reported here was accomplished by irradiating strips with 10 serial laser pulses with a simulated total duration of (27.9 + 9 × 13.8) ns which rounds to ~152 ns. Estimates of the mass lost during 10 laser pulses, derived both from a rivulet and particle array, suggests a mass reduction of ~24 and 18%, respectively (2.4 and 1.8% per pulse, ESI 2†). These percent reductions are consistent with our previous results using copper.[26] The low mass loss is consistent with the fact that we are at a much lower fluence than the measured ablation threshold of 900 mJ cm^{-2} (for 248 nm wavelength) which minimizes the mass lost by vaporization.[40]

For convenience, we consider the moment of rivulet formation as the time origin ($t = 0$) for the modified RP instability to develop. The calculated rivulet formation time (illustrated in Fig. 1b blue strip transforming to green rivulet) of 27.1 ns during the first laser pulse was based on the experimentally measured, mean edge retraction velocity of ~16 ± 6 nm ns^{-1}. Thus, the instability was estimated to develop over a time of (27.9 − 27.1 + 9 × 13.8) ns which rounds to 125 ns. *A key element to our directed assembly model is the translation of the synthetic perturbation from the thin film strip to the rivulet* (Fig. 1b). *The large amplitude imparted to this mode ultimately dictates the rivulet breakup pattern leading to re-solidified droplets* (Fig. 1b red features).

Synthetic mode transfer from the thin film strip edges to the transaxial radial dimension of the rivulet can be seen in the top-down SEM image of a re-solidified Ni rivulet, supported on a SiO_2 substrate, after pulsed laser melting (Fig. 1c). The relatively darker region surrounding the rivulet indicates the original position of contact between the thin film strip and the SiO_2 surface. The SEM image in Fig. 1c demonstrates the specific case of the development of a stable mode with a negative growth rate ($\omega < 0$) where the amplitude is expected to decay with time once the rivulet forms. This effect can be observed in the image where the amplitude of the stable mode on the rivulet surface is smaller than the amplitude initially imposed on the thin film strip. The time expected for the amplitude of this mode to completely decay is calculated later.

Thin film strip geometries were explored to facilitate the parallel assembly of both linear particle chains and continuous

wires precisely positioned along a common rivulet (Fig. 1d). *This goal was accomplished by tailoring the wavelength and amplitude of unstable modes in order to control stability/instability.* Fig. 1d shows the original lithography design for the thin film strip which yielded parallel assembly. The fastest growing mode $\lambda_m = 0.970 \pm 0.015$ μm was prescribed along the thin film strip edge with an initial amplitude (A_o) of 50 ± 7 nm and is seen clearly as the patterned oscillation. Fig. 1a (green line) indicates that the growth rate of the 0.970 μm mode is 0.040 ns^{-1} according to the LSA.[15,41] This portion of the thin film strip was designed to yield linear particle chains following rivulet formation and breakup for two reasons; (1) 0.970 μm is the fastest growing mode and (2) the relatively large amplitude of 50 nm accelerates breakup relative to the straight, unperturbed sections of the strip. Conversely, the straight, unperturbed portions of the strip were designed to yield rivulets, or wires. Control over the *solid phase* breakup on substrates has recently been demonstrated by Thompson and Ye[42] where the single crystal orientation of the underlying substrates plays a key role in directed assembly.

A comparison of the straight edge and synthetic perturbation dynamics reveals the time window available for the parallel assembly. The fastest growing mode of 0.970 μm will develop on the straight, unperturbed portion of the strip (*all unstable modes actually develop simultaneously but it is the most rapid evolving mode that sets the lower limit of the breakup time*). The evolution of this mode is significantly delayed relative to the patterned one due to the strong dependence of breakup time on the initial perturbation amplitude. An estimate of the characteristic breakup, or decay, time (τ) for a rivulet of radius R_o, wetting angle θ, wavelength λ and with an initial amplitude A_o is;

$$\tau = \frac{1}{\omega(\lambda)} \ln \frac{w_{1/2}(0,\tau) - R_o \sin\theta}{A_o} \quad (2)$$

Eqn (2) is described in more detail in ESI 3† and is an approximation, since we are assuming that the linear stability analysis is valid all the way until breakup. $w_{1/2}(l,t)$ is defined to be the time-dependent half-width of the rivulet amplitude at the peak of a perturbation; the moment of breakup occurs when $w_{1/2}(0,\tau) = 2R_o \sin\theta$.

A lithographically defined varicose perturbation provides a "head-start" toward breakup relative to a straight edge pattern (Fig. 1d and e). Conversely, a smooth rivulet, produced by melting an *unperturbed* strip, must rely on the evolution of very small amplitude, naturally evolving oscillations for breakup. A_o is assumed to be 1 nm for this case. Eqn (2) yields an estimated breakup time of 116 ns after rivulet formation for the straight edged portions of the rivulet ($\lambda = 0.970$ μm, $A_o = 1$ nm). In contrast, the synthetic perturbation is estimated to have a shorter breakup time of 18 ns when using $\lambda = 0.970$ μm and $A_o = 50$ nm. *Thus, the difference between these two values for break-up (116 − 18 = 98 ns) sets the nanosecond time range available to yield droplets in the perturbed sections and wires in the previously straight edged sections.* Fig. 1d shows the results of such an experiment where the total rivulet liquid lifetime was calculated to be 125 ns. The originally perturbed ($A_o = 50$ nm) sections of the rivulet have formed particles as predicted by the 18 ns breakup time. Also consistent with calculations, the originally straight-edged portions of the thin film strip have formed the wire morphology. However, some disagreement exists between calculations and experiments. For example, calculations suggest that particle evolution should have begun at 116 ns where the strip was originally defined with straight edges. We address the source of this difference below. It is important to mention here that the retraction of the rivulet ends must be considered in certain cases (according to the Ohnesorge number $Oh = v/(\rho\gamma L)^{1/2}$, where L is the characteristic dimension and ρ is the liquid density) although here such retraction had negligible influence on the final particle and wire placement.[43]

The experimental breakup time was found to increase with wavelength as predicted by the dispersion curve (Fig. 1a) in the long wavelength regime. To demonstrate this fact, a series of strips were patterned with wavelengths longer than the wavelength of maximum growth rate (λ_m). The perturbation amplitude was fixed. The strips were simultaneously exposed to 10 laser pulses using a per pulse fluence of 220 mJ cm^{-2}. Post-exposure images shown in Fig. 2 reveal a clear trend between the perturbation wavelengths (labeled at right) and their growth rates. As the wavelength was increased from 950 nm (close to λ_m) a transition was observed from saturated nanoparticles to a premature morphology of fragmented rivulets at longer wavelengths. These experiments show the dynamics of the perturbation evolution and that different particle spacings/sizes may be controllably produced. Thus, one can appropriately vary the geometry of the initial strip by varying the width and/or thickness

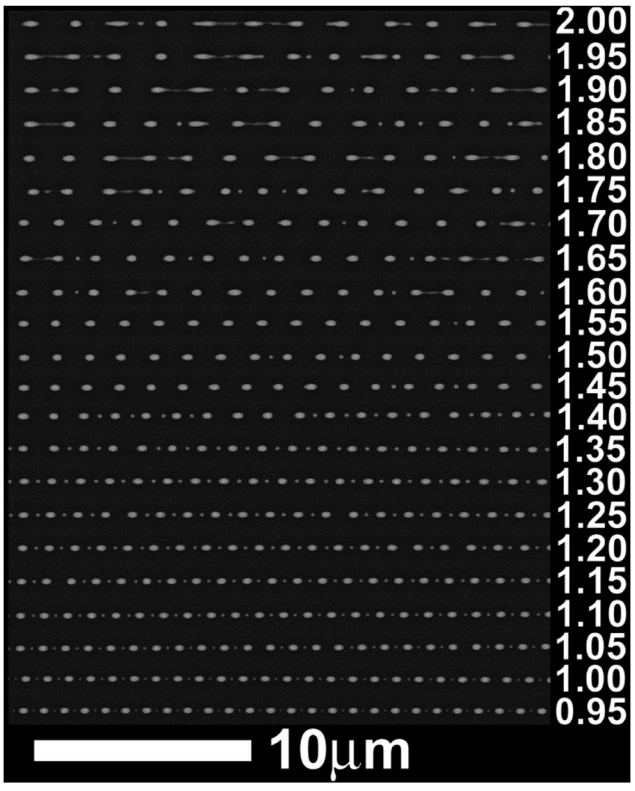

Fig. 2 Nickel particle development as a function of synthetic perturbation wavelength. Each row of particles started as a horizontally oriented thin film strip. The initial wavelength of the thin film strip perturbation is shown to the right for each row of particles. A constant photon fluence of 220 mJ cm^{-2} and 10 pulses were applied to each strip. Each strip had a thickness of 10 nm and an average width of 1.10 μm. The unstable wavelength regime of 0.95–2.00 μm was explored in steps of 50 nm.

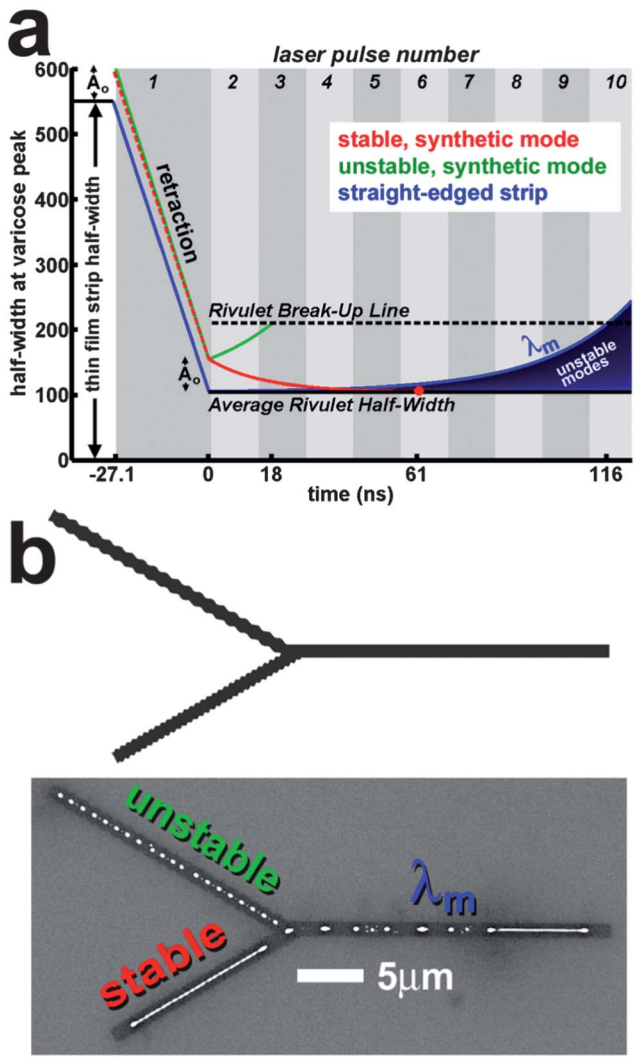

Fig. 3 Nickel half-width development as a function of time. Half-width development is shown in each case at the varicose maximum peak position. Development is shown starting from the initial thin strip morphology and ending at breakup. Rivulet development was estimated using eqn (2), ESI 3.† The plotted results depended strongly on the predicted modal growth rates as derived from linear stability analysis. (a) The cases of synthetic and unstable (green line), synthetic and stable (red line) and unperturbed, straight strip (blue line) evolution are shown in the plot. Thin film strip edge retraction occurs at nearly constant velocity (16 ± 6 m s^{-1}) according to experimental results (not shown) explaining the linear slope of varicose maximum peak position *versus* time during the first laser pulse. Simulations suggested a liquid lifetime of 27.9 ns during the initial laser pulse where the 10 nm thick Ni film was irradiated using a fluence of 220 mJ cm^{-2} (ESI 1†). Based on this retraction velocity, rivulet formation occurred at ~1 ns before the end of the liquid lifetime for the 1st pulse. Subsequent laser pulses irradiated the rivulet morphology yielding a liquid lifetime of 13.8 ns per pulse. The 0.970 μm ($A_o = 50$ nm) synthetic perturbation (green line) was estimated to breakup 18 ns after rivulet formation or during the 3rd laser pulse. The 0.970 μm wavelength was also the fastest growing mode and thus set the lower limit of the breakup time for the case of the unperturbed rivulet (blue line). Yet, due to the lack of a prescribed amplitude, the starting amplitude was assumed to be 1 nm. This reduced amplitude delayed breakup to 116 ns for the naturally developing 0.970 μm mode. The synthetic, stable mode of 0.500 μm must first decay, which is predicted to occur after 61 ns, before unstable mode propagation can begin. (b) The computer aided design of a Ni thin film strip, 10 nm thick, including three branches. Each branch is the experimental complement to the predictions shown in (a). A plethora of unstable modes may propagate, simultaneously with the fastest growing mode, and these are indicated by the shaded blue region.

to align the synthetic perturbation wavelength with the wavelength of maximum growth rate to yield particles with this spacing. As a result, the parallel assembly time window may be maximized, *e.g.*, relative to the breakup time for a straight edge thin film strip, by matching the synthetic perturbation wavelength and wavelength of maximum growth rate. Thus, parallel assembly can be used over a range of wavelengths while ensuring the largest possible parallel assembly time window.

A convenient way to visualize the dynamics of the parallel assembly process is to compare the half-width at the perturbation peaks as a function of time. Fig. 3a shows an estimate of the half-width evolution at the perturbation peak position, starting with the mean thin film strip half-width and ending at breakup, for the synthetic 0.970 μm mode (green line) with $A_o = 50$ nm and the straight edge strip (blue line) with $A_o = A_i = 1$ nm. As shown, the initial rivulet formation times are basically the same, however the synthetic unstable mode has a much larger amplitude relative to the naturally evolving wave (50 nm *versus* 1 nm) leading to the faster development in the synthetically perturbed regions. The calculated minimum time range available for parallel assembly of particles and wires extends from 18 ns to 116 ns as shown in Fig. 3a.

The parallel assembly time range can be extended even further by implementing a combination of unstable and stable growth modes. This conclusion is based on the experimental observation that stable modes must first decay, producing a smooth rivulet, followed by the development of the RP instability according to the fastest growing mode (λ_m). For example, Fig. 3b shows a thin film strip feature that had both a synthetic, stable branch and a straight-edged branch. Following irradiation, the unstable synthetic perturbations are fully developed with precise particles, as expected. The straight-edged branch has partially fragmented while the stable branch is still in the rivulet stage. The straight-edged branch shows an incomplete development with the formation of particles near the junction and intermediate fragmentation on the other end which is characteristic of finite length rivulets.[44] Although we anticipate that a plethora of naturally evolving unstable modes should ultimately develop simultaneously in the stable, synthetic mode section, it seems that the stable mode interferes with the development of these modes. Thus, we anticipate that the breakup time for the stable, synthetic strip depends on the consecutive events including (1) the decay from the synthetic amplitude and (2) the time required for the fastest growing mode to evolve to breakup.

Returning to eqn (2), stable mode ($\lambda = 500$ nm) amplitude decay is complete when $w_{1/2}(l = 0,\tau) = A_i + R_o \sin\theta$ and the negative growth rate of -0.068 ns^{-1} (Fig. 1a, red line) yields an amplitude decay time of 61 ns (from 50 nm to 1 nm). Next, the λ_m mode should evolve, and as we have shown, takes ~116 ns to induce breakup. Thus, the total liquid lifetime required to yield breakup should be ~116 + 61 = 167 ns. Fig. 1c demonstrates that the stable mode appears to still be in the decay stage at the experimental cumulative rivulet liquid lifetime of 125 ns. However, Fig. 3a (red

line) suggests that the complete decay of the stable mode should have happened at 61 ns. We should recall however that linear stability analysis tends to underestimate the breakup time, since it assumes that initial (exponential) growth of a perturbation persists all the way to the breakup; nonlinear effects tend to slow down this growth and lead to longer breakup times. Nonetheless, using the stable, synthetic mode, the parallel assembly time window has been greatly increased for the case of the stable mode, relative to the case of a straight, unperturbed thin film strip.

Conclusions

The directed and simultaneous assembly of Ni wires and particles on a SiO_2-coated substrate was demonstrated. The initial Ni thin film strip pattern, fabricated by electron beam lithography and sputter metallization, was designed to yield this result by prescribing nanoscale, sinusoidal perturbations on the lengthwise edges of the strip. Pulsed laser melting of the Ni film induced the morphological and liquid-phase transformation into a rivulet, with the perturbations transferred onto the rivulet surface in the form of a varicose oscillation. Linear stability analysis predicted both the instability and growth of the varicose wave spectrum based on the rivulet material, radius and contact angle with respect to the substrate. From this information, it was possible to affect the stability of the rivulet by controlling the wavelength and amplitude of the initial edge defined perturbation. The fastest developing varicose mode with a large, prescribed amplitude acted to effectively accelerate rivulet breakup along select portions to the rivulet/wire facilitating particle formation while straight-edged regions or regions with wavelengths promoting stability developed slowly. Ultimately, a finite liquid lifetime range existed during which both particles and wires could be formed. The nanosecond pulse width of the laser facilitated the rapid quenching of this morphology yielding solid phase Ni wires and particles. In principle, the method can be extended to promote wire and particle formation in a host of metal film-dielectric substrates systems provided; (1) T_m(metal) < T_m(substrate), (2) film thicknesses are on the order of 30 nm or less and (3) chemical interactions between the metal and substrate are limited.

Acknowledgements

J. Fowlkes., Y. Wu and P. Rack acknowledge support from the U.S. Department of Energy, Basic Energy Sciences, Materials Sciences and Engineering Division for supporting the experimental portions of this work related to the pulsed laser irradiation of thin films and understanding the fundamental mechanisms operative during liquid phase, thin film dewetting. J. Diez, P. Rack and J. Fowlkes also acknowledge that the lithography and electron imaging results reported in this paper were conducted at the Center for Nanophase Materials Sciences, which is sponsored at Oak Ridge National Laboratory by the Scientific User Facilities Division, Office of Basic Energy Sciences, U. S. Department of Energy. L. Kondic acknowledges support by the NSF grant no. DMS-0908158. J. Diez and A. González acknowledge CONICET – Argentina for travel support within the International Cooperation Program and ANPCyT – Argentina for support within the project PICT 2498/06.

References

1 C. D. Fernández, G. Mattei, E. Paz, R. L. Novak, L. Cavigli, L. Bogani, F. J. Palomares, P. Mazzoldi and A. Caneschi, *Nanotechnology*, 2010, **21**, 165701.
2 M. T. Rahman, N. N. Shams and C. H. Lai, *J. Appl. Phys.*, 2009, **105**, 07C112.
3 Y. J. Oh, S. G. Park, M. H. Kang, J. H. Choi, Y. Nam and K. H. Jeong, *Small*, 2011, **7**, 184–188.
4 H. Song, M. A. Reed and T. Lee, *Adv. Mater.*, 2011, **23**, 1583–1608.
5 H. A. Atwater and A. Polman, *Nat. Mater.*, 2010, **9**, 205–213.
6 K. R. Catchpole and A. Polman, *Appl. Phys. Lett.*, 2008, **93**, 191113.
7 S. Y. Chou, P. R. Krauss and P. J. Renstrom, *Science*, 1996, **272**, 85–87.
8 T. G. Leong, A. M. Zarafshar and D. H. Gracias, *Small*, 2010, **6**, 792–806.
9 J. H. Cho, M. D. Keung, N. Verellen, L. Lagae, V. V. Moshchalkov, P. Van Dorpe and D. H. Gracias, *Small*, 2011, **7**, 1943–1948.
10 P. Nagpal, N. C. Lindquist, S. H. Oh and D. J. Norris, *Science*, 2009, **325**, 594–597.
11 Y. Cui, M. T. Bjork, J. A. Liddle, C. Sonnichsen, B. Boussert and A. P. Alivisatos, *Nano Lett.*, 2004, **4**, 1093–1098.
12 B. Cui, C. Keimel and S. Y. Chou, *Nanotechnology*, 2010, **21**, 045303.
13 S. Y. Chou and Q. F. Xia, *Nat. Nanotechnol.*, 2008, **3**, 369.
14 J. D. Fowlkes, L. Kondic, J. Diez, Y. Y. Wu and P. D. Rack, *Nano Lett.*, 2011, **11**, 2478–2485.
15 L. Kondic, J. A. Diez, P. D. Rack, Y. F. Guan and J. D. Fowlkes, *Phys. Rev. E: Stat., Nonlinear, Soft Matter Phys.*, 2009, **79**, 026302.
16 J. D. Fowlkes, Y. Y. Wu and P. D. Rack, *ACS Appl. Mater. Interfaces*, 2010, **2**, 2153–2161.
17 H. G. Duan and K. K. Berggren, *Nano Lett.*, 2010, **10**, 3710–3716.
18 W. A. Lopes and H. M. Jaeger, *Nature*, 2001, **414**, 735–738.
19 J. Henzie, J. E. Barton, C. L. Stender and T. W. Odom, *Acc. Chem. Res.*, 2006, **39**, 249–257.
20 J. Henzie, M. H. Lee and T. W. Odom, *Nat. Nanotechnol.*, 2007, **2**, 549–554.
21 J. H. Cho, A. Azam and D. H. Gracias, *Langmuir*, 2010, **26**, 16534–16539.
22 J. H. Cho and D. H. Gracias, *Nano Lett.*, 2009, **9**, 4049–4052.
23 M. H. Lee, J. Y. Lin and T. W. Odom, *Angew. Chem., Int. Ed.*, 2010, **49**, 3057–3060.
24 Y. Wu, J. D. Fowlkes and P. D. Rack, *J. Mater. Res.*, 2011, **26**, 277–287.
25 Y. Wu, J. D. Fowlkes, P. D. Rack, J. A. Diez and L. Kondic, *Langmuir*, 2010, **26**, 11972–11979.
26 Y. Wu, J. D. Fowlkes, N. A. Roberts, J. A. Diez, L. Kondic, A. G. González and P. D. Rack, *Langmuir*, 2011, **27**, 13314–13323.
27 F. Brochard-Wyart and C. Redon, *Langmuir*, 1992, **8**, 2324–2329.
28 K. Sekimoto, R. Oguma and K. Kawasaki, *Ann. Phys.*, 1987, **176**, 359–392.
29 J. A. Diez, A. G. González and L. Kondic, *Phys. Fluids*, 2009, **21**, 082105.
30 L. Rayleigh, *Philos. Mag.*, 1892, **34**, 145–154.
31 J. A. F. Plateau, *Mem. Acad. Sci. Brux.*, 1843, **16**, 3.
32 Q. F. Xia and S. Y. Chou, *Nanotechnology*, 2009, **20**, 285310.
33 S. J. Henley, J. D. Carey and S. R. P. Silva, *Phys. Rev. B: Condens. Matter Mater. Phys.*, 2005, **72**, 195408.
34 J. Lian, L. M. Wang, X. C. Sun, Q. K. Yu and R. C. Ewing, *Nano Lett.*, 2006, **6**, 1047–1052.
35 P. Kumar, *Nanoscale Res. Lett.*, 2010, **5**, 1367–1376.
36 Q. F. Xia and S. Y. Chou, *Appl. Phys. A: Mater. Sci. Process.*, 2010, **98**, 9–59.
37 J. G. Hagedorn, N. S. Martys and J. F. Douglas, *Phys. Rev. E: Stat., Nonlinear, Soft Matter Phys.*, 2004, **69**, 056312.
38 A. R. Kortan and R. L. Park, *Phys. Rev. B: Condens. Matter Mater. Phys.*, 1981, **23**, 6340–6347.
39 P. D. Rack, Y. Guan, J. D. Fowlkes, A. V. Melechko and M. L. Simpson, *Appl. Phys. Lett.*, 2008, **92**, 223108.
40 X. Xu and K. Song, *Appl. Phys. A: Mater. Sci. Process.*, 1999, **69**, S869–S873.
41 J. A. Diez and L. Kondic, *Phys. Fluids*, 2007, **19**, 072107.
42 J. Ye and C. V. Thompson, *Adv. Mater.*, 2011, **23**, 1567–1571.
43 A. A. Castrejón-Pita, J. R. Castrejón-Pita and I. M. Hutchings, *Phys. Rev. Lett.*, 2012, **108**, 074506.
44 J. A. Diez, A. G. González and L. Kondic, *Phys. Fluids*, 2012, **24**, 032104.

